nature photonics

LETTERS

https://doi.org/10.1038/s41566-019-0475-6

THz-to-optical conversion in wireless communications using an ultra-broadband plasmonic modulator

S. Ummethala[1,2*], T. Harter[1,2], K. Koehnle[1,2], Z. Li[1], S. Muehlbrandt[1,2], Y. Kutuvantavida[1,2], J. Kemal[1], P. Marin-Palomo[1], J. Schaefer[3], A. Tessmann[4], S. K. Garlapati[5], A. Bacher[2], L. Hahn[2], M. Walther[4], T. Zwick[3], S. Randel[1], W. Freude[1] and C. Koos[1,2*]

Future wireless communication networks will need to handle data rates of tens or even hundreds of Gbit s^{-1} per link, requiring carrier frequencies in the unallocated THz spectrum[1,2]. In this context, seamless integration of THz links into existing fibre-optic infrastructures[3] is of great importance to complement the inherent portability and flexibility advantages of wireless networks and the reliable and virtually unlimited capacity of optical transmission systems. On the technological level, this requires novel device and signal processing concepts for direct conversion of data streams between the THz and optical domains. Here, we demonstrate a THz link that is seamlessly integrated into a fibre-optic network using direct THz-to-optical (T/O) conversion at the wireless receiver. We exploit an ultra-broadband silicon-plasmonic modulator having a 3 dB bandwidth in excess of 0.36 THz for T/O conversion of a 50 Gbit s^{-1} data stream that is transmitted on a 0.2885 THz carrier over a 16-m-long wireless link. Optical-to-THz (O/T) conversion at the wireless transmitter relies on photomixing in a uni-travelling-carrier photodiode.

Data traffic in wireless communication networks is experiencing explosive growth[4] and will account for more than 60% of the overall Internet traffic by 2021. To cope with the associated capacity challenges, wireless communication networks will need to exploit frequency windows of low atmospheric attenuation in the unallocated THz spectrum beyond 0.275 THz (ref. [1]). Moreover, intimate integration of future wireless links into fibre-optic infrastructures will be of crucial importance, for example in THz-over-fibre (ToF)[3] or fibre-to-the-antenna[5] architectures. This requires seamless connections between optical fibres and wireless THz communication front-ends.

At the THz transmitter (Tx), optoelectronic conversion of data signals from the optical domain to the THz domain has been shown to offer a variety of advantages[1] over conventional all-electronic approaches. These advantages include wideband tunability of the THz carrier frequency and the opportunity to utilize advanced optical circuitry for generation and multiplexing of data streams before conversion to the THz domain. Wireless transmission with data rates of 100 Gbit s^{-1} or more has previously been demonstrated[6–8] by using ultra-fast uni-travelling-carrier[9] (UTC) photodiodes for direct O/T conversion of wavelength-division multiplexing (WDM) signals. In contrast to that, direct T/O conversion of data streams at the receiver (Rx) has not yet been demonstrated, and previous transmission experiments[6–8,10–12] relied on all-electronic downconversion of the signals to the baseband using, for example, sub-harmonic mixers[13] or Schottky diodes[14].

In this Letter, we demonstrate a wireless THz link that is seamlessly integrated into a photonic network, complementing direct O/T conversion at the THz Tx by direct T/O conversion at the THz Rx. The wireless link operates at line rates of up to 50 Gbit s^{-1}, transmitted at a carrier frequency of 0.2885 THz over a distance of 16 m. The THz signal is generated by O/T conversion in a UTC photodiode. At the receiver, the THz signal is converted to the optical domain by means of an ultra-broadband plasmonic–organic hybrid (POH) modulator. The POH modulator features a flat frequency response[15,16] up to 0.36 THz along with small footprint of about 600 μm^2, thus lending itself to high-density photonic integration. To the best of our knowledge, this is the first demonstration of direct conversion of a wireless data signal from a THz carrier to the optical domain without downconversion to the baseband or to an intermediate frequency. We expect that the combination of direct O/T and T/O conversion in ultra-compact devices has the potential to greatly accelerate THz communications and to advance the integration of THz wireless links into fibre-optic infrastructures.

Figure 1a illustrates the concept of a future communication network that combines geographically distributed THz transceiver (TRx) front-ends with powerful centralized digital signal processing (DSP) sites. The wireless TRx front-ends and the DSP sites are connected through widely deployed fibre-optic network infrastructures that exploit optical carriers to efficiently carry analogue data signals over large distances. The architecture relies on direct O/T and T/O conversion at the TRx front-end, which is key to efficiently interface optical fibres to THz antennas. Direct conversion between analogue optical signals and THz waveforms considerably reduces the complexity at the antenna site and improves scalability to a large number of geographically distributed high-performance THz links or cellular networks. Similarly, the concept of moving computationally expensive digital processing of baseband (BB) signals to centralized sites such as large-scale data centres offers unprecedented network

[1]Institute of Photonics and Quantum Electronics (IPQ), Karlsruhe Institute of Technology (KIT), Karlsruhe, Germany. [2]Institute of Microstructure Technology (IMT), Karlsruhe Institute of Technology (KIT), Eggenstein-Leopoldshafen, Germany. [3]Institute of Radio Frequency Engineering & Electronics (IHE), Karlsruhe Institute of Technology (KIT), Karlsruhe, Germany. [4]Fraunhofer Institute for Applied Solid State Physics (IAF), Freiburg, Germany. [5]Institute of Nanotechnology (INT), Karlsruhe Institute of Technology (KIT), Eggenstein-Leopoldshafen, Germany. *e-mail: sandeep.ummethala@kit.edu; christian.koos@kit.edu

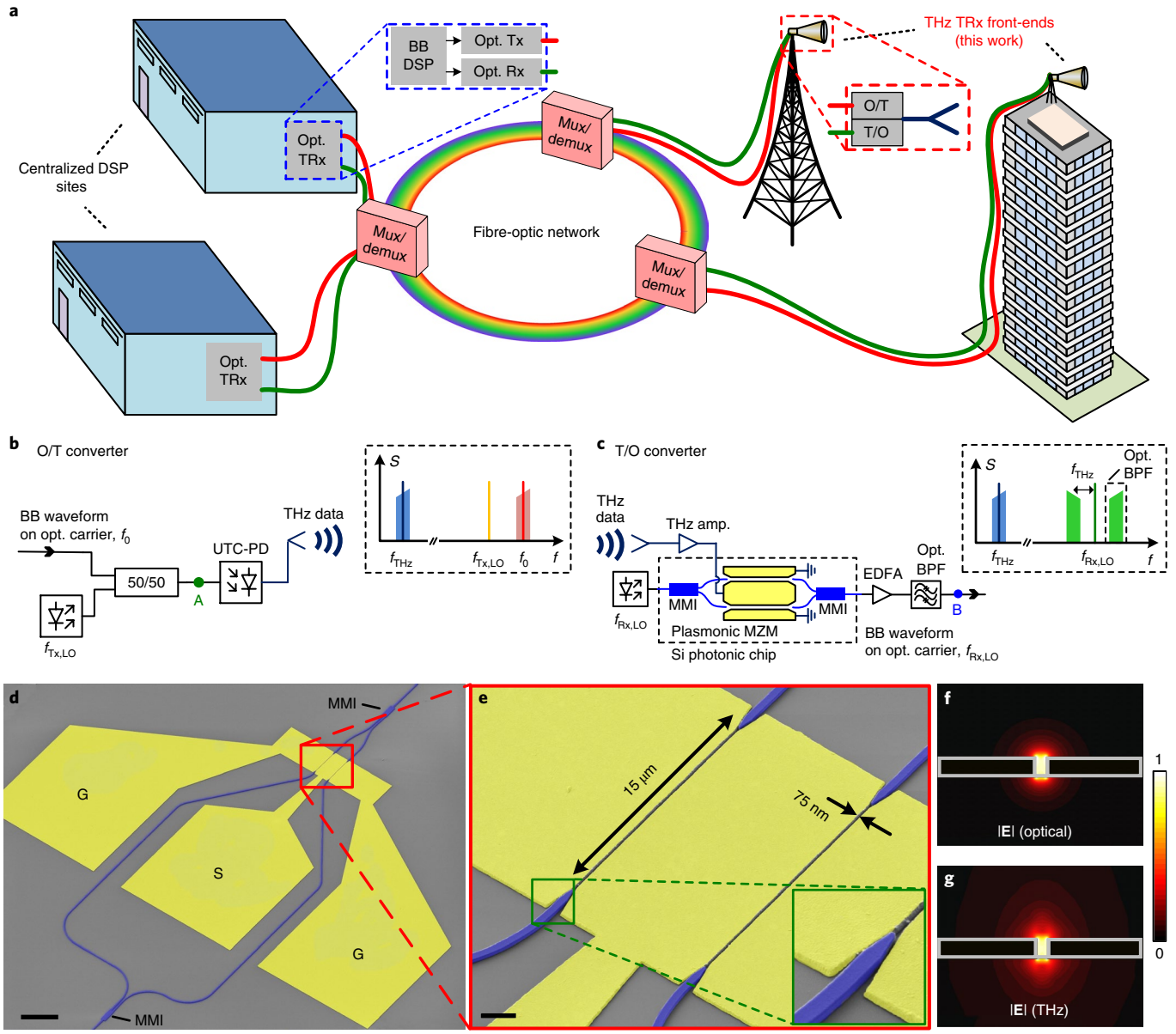

Fig. 1 | Seamless integration of THz wireless links into fibre-optic infrastructures by direct O/T and T/O conversion. a, Vision of a future communication network architecture that combines geographically distributed analogue TRx front-ends with powerful centralized DSP sites through fibre-optic network infrastructures. Our work focuses on direct T/O and O/T conversion of analogue waveforms at the THz front-end, which allows us to efficiently interface optical fibres to THz antennas. This considerably reduces complexity at the antenna site and improves scalability to a large number of THz links or cellular networks. The envisaged concept may thus represent a key step towards overcoming the capacity bottlenecks in wireless communication infrastructures. Mux/demux, multiplexer/demultiplexer. **b**, Concept of direct O/T conversion. The baseband (BB) waveform is first modulated onto an optical carrier at frequency f_0 and sent to the O/T converter. The optical signal is then translated to a THz carrier by photomixing with a c.w. local oscillator (LO) laser tone at a frequency $f_{Tx,LO}$ in an ultra-fast UTC photodiode (UTC-PD). The THz data signal is radiated into free space by an antenna. Inset: optical data spectrum (centre frequency f_0), LO tone (frequency $f_{Tx,LO}$) and THz spectrum (centre frequency f_{THz}) after O/T conversion. **c**, Concept of direct T/O conversion. The THz data signal is received by an antenna, amplified by a THz amplifier, and then fed to a plasmonic MZM for modulation onto a c.w. carrier at optical frequency $f_{Rx,LO}$. After modulation, the optical signal from the MZM contains an upper and a lower modulation sideband. An optical BPF is used to suppress the carrier and to select one of the modulation sidebands. Inset: illustration of the spectrum of the THz signal (carrier frequency f_{THz}) along with the optical LO tone (frequency $f_{Rx,LO}$) and the optical signal sidebands generated by THz modulation. The BPF is configured to select one of the sidebands (centre frequency $f_{Rx,LO}+f_{THz}$). **d**, False-coloured SEM image of a plasmonic MZM with GSG contact pads (yellow) and silicon photonic waveguides (blue). Scale bar, 20 µm. **e**, Zoom-in of the plasmonic section of the MZM showing two 15-µm-long phase modulators with photonic-to-plasmonic mode converters (inset). Scale bar, 2 µm. Each section consists of a plasmonic slot waveguide, featuring a 75-nm-wide gap between two extended gold pads (yellow). **f**,**g**, Field profile of the optical quasi-TE mode (**f**) and the THz field (**g**). Both figures indicate the magnitudes of the complex electric field vectors. Note that the optical and electrical modes are tightly confined to the slot region, thereby ensuring strong interaction and efficient modulation.

scalability, flexible and efficient sharing of crucial resources, as well as improved network resilience. Seamless combination of short-reach THz links with long-reach fibre-optic networks may thus represent a key step towards overcoming the capacity bottlenecks in wireless communication infrastructures. Note that the scheme presented here is mainly geared towards wireless THz connections

between fixed transmitter and receiver stations rather than towards serving mobile terminals, for which steered THz beams would be required.

At its heart, the architecture depicted in Fig. 1a relies on THz transmitter (Tx) and receiver (Rx) front-ends that allow for direct conversion between optical and THz signals. The underlying concepts are illustrated in Fig. 1b,c. After generating the analogue baseband waveform of the data signal at the DSP site, it is modulated onto an optical carrier at frequency f_0 by an optical transmitter (Opt. Tx) and then sent to the THz Tx through a fibre-optic network. At the THz Tx (Fig. 1b), the optical signal is then converted to a THz waveform by photomixing with a continuous-wave (c.w.) local oscillator (LO) tone at frequency $f_{\mathrm{Tx,LO}}$ in a UTC photodiode (inset, Fig. 1b). The THz data signal, centred at the difference frequency $f_{\mathrm{THz}} = |f_{\mathrm{Tx,LO}} - f_0|$, is then transmitted into free space by an antenna. At the T/O converter (Fig. 1c), the THz data signal is received by another antenna and fed to a THz amplifier. For conversion to an optical carrier, the amplified signal is then coupled to a POH[17–23] Mach–Zehnder modulator (MZM), which is fed by an optical carrier at frequency $f_{\mathrm{Rx,LO}}$. The POH MZM generates an upper and a lower modulation sideband. An optical band-pass filter (BPF) is used to suppress the carrier and to select one of the modulation sidebands (inset, Fig. 1c). This scheme allows for operation over a wide range of THz frequencies, and does not require any downconversion to an intermediate frequency before encoding the data onto an optical carrier, and hence considerably reduces the complexity at the THz front-end. After T/O conversion, the analogue signal is sent back through the fibre-optic network to an optical receiver (Opt. Rx) in the centralized DSP site. The scheme illustrated in Fig. 1c crucially relies on ultra-broadband electro-optic (EO) modulators, offering modulation bandwidths that extend into the THz spectrum. High-speed MZMs have previously been demonstrated using lithium niobate as the EO medium—either as bulk material[24] or as thin films on silicon[25] or quartz[26] substrates. However, these devices are usually realized in a travelling-wave configuration with typical device lengths on the millimetre or centimetre scale, which is not well suited for high-density integration. Moreover, while some lithium niobate devices show measurable sidebands up to modulation frequencies[26] of 0.5 THz, the underlying 3 dB bandwidths[24–26] are so far limited to ~0.1 THz. These bandwidth limitations can be overcome by POH modulators[17–23] that combine organic EO materials with ultra-compact plasmonic slot waveguides[27–29]. The POH concept allows considerably reducing the device footprint and offers a route towards high-density co-integration[22] with advanced silicon photonic circuitry[30,31]. A fabricated POH MZM is shown in the false-coloured scanning electron microscope (SEM) image in Fig. 1d. Light is coupled to the silicon photonic (SiP) chip via on-chip grating couplers (not shown) and propagates in silicon strip waveguides (blue) as a quasi-transverse-electric (quasi-TE) mode. A multimode interference (MMI) coupler splits the light from the input waveguide and launches it into the two arms of an unbalanced MZM. A second MMI at the other end of the MZM combines the modulated signals into an output waveguide, which is connected to another grating coupler. Each arm of the MZM contains a POH phase modulator section comprising a narrow metallic slot (width $w = 75$ nm) between the gold electrodes (yellow, Fig. 1e). A pair of tapered silicon waveguides in each arm is used to convert[32] the photonic mode of the silicon strip waveguide to the surface plasmon polariton (SPP) mode in the metallic slot waveguide and vice versa (inset, Fig. 1e). The slots are filled with the organic EO material[33] SEO100. A THz signal applied to the ground-signal-ground (GSG) contacts of the POH MZM leads to a THz electric field in the slots of each of the two arms and thus creates an optical phase shift. Figure 1f,g shows that both the optical quasi-TE field and the THz electric field are tightly confined to the metallic slot region, leading to strong overlap and a high modulation efficiency. The MZM is configured to operate in push–pull mode with phase shifts of equal magnitude but opposite signs in each arm. This is accomplished by an appropriate choice of the poling directions[34] of the EO material with respect to the modulating THz field inside the two slot waveguides. Further details on the device fabrication are provided in the Methods.

Due to the strong interaction of the THz field and the optical field in the metallic slot waveguide, POH phase shifters can be very short. This leads to ultra-small parasitic capacitances of the order of a few fF, thereby permitting theoretical *RC* cutoff frequencies in excess of 1 THz when connected to a signal source with a 50 Ω internal impedance[18,34]. For our experiments, we fabricated a 15-μm-long POH MZM with a slot width of 75 nm and characterized its response over an extended frequency range of up to 0.36 THz, limited by the signal sources available in our laboratory. Figure 2a shows the basic set-up for the bandwidth measurement. The optical c.w. carrier at frequency f_c is derived from an external-cavity laser (ECL) and launched into the POH MZM, which is driven by a small sinusoidal RF or THz signal with varying drive frequency f_m. The intensity-modulated optical signal is then amplified by an erbium-doped fibre amplifier (EDFA) and detected by an optical spectrum analyser to evaluate the phase modulation index $\eta(f_m)$. Due to the small electrical drive powers of the THz sources in combination with the comparatively high insertion loss of the specific POH MZM used in our experiments, an EDFA was necessary to boost the optical output power for these measurements. The EDFA could be omitted for later device generations with reduced insertion loss (see Supplementary Section I for details). For each drive frequency, the optical spectrum exhibits a peak at f_c along with two first-order sidebands at $f_c \pm f_m$. Assuming that the MZM is biased at its quadrature (3 dB) point and that both arms of the MZM have the same phase modulation index η, the sideband-to-carrier power ratio $R_{1,0}$ allows us to calculate η according to the relation[35] $R_{1,0} \approx \eta^2/4$ for small amplitude of the drive signal ($\eta \ll 1$) (see Methods and Supplementary Section I for more details). Note that the electric drive power P_e provided by our signal source shows a strong dependency on the modulation frequency f_m. Given that the phase modulation index η is proportional to the electric drive voltage U_e, we can eliminate the impact of the frequency-dependent drive power $P_e(f_m)$ by considering the ratio $\eta(f_m)/U_e(f_m)$. Normalizing the frequency characteristic of this ratio to its value at a reference modulation frequency of $f_{m,ref} = 2$ GHz, we obtain the dimensionless normalized phase modulation index

$$\eta_U(f_m) = 20\log_{10}\left(\frac{\eta(f_m)/U_e(f_m)}{\eta(f_{m,ref})/U_e(f_{m,ref})}\right) \quad (1)$$

Raw data and details on the evaluation are provided in Supplementary Section I. The results obtained for our 15-μm-long POH MZM are shown in Fig. 2b. The device features a flat frequency response over the entire measurement range with no indication of any frequency-dependent decay. The noticeable variations of approximately ±2.5 dB in the frequency response are attributed to uncertainties of our measurement technique and do not represent an intrinsic property of the POH MZM (see Supplementary Section I for details).

The experimental results hint at a 3 dB bandwidth that is significantly larger than the highest measured frequency of 0.36 THz. To the best of our knowledge, this represents the fastest EO modulator that has so far been published. Our findings are well in line with earlier demonstrations of POH modulators, where operation up to frequencies of 0.17 THz has been shown[23]. Note that POH devices are not limited to gold as a plasmonic material, but may also be realized by employing CMOS-compatible materials[36], which would allow for co-integration with CMOS electronics.

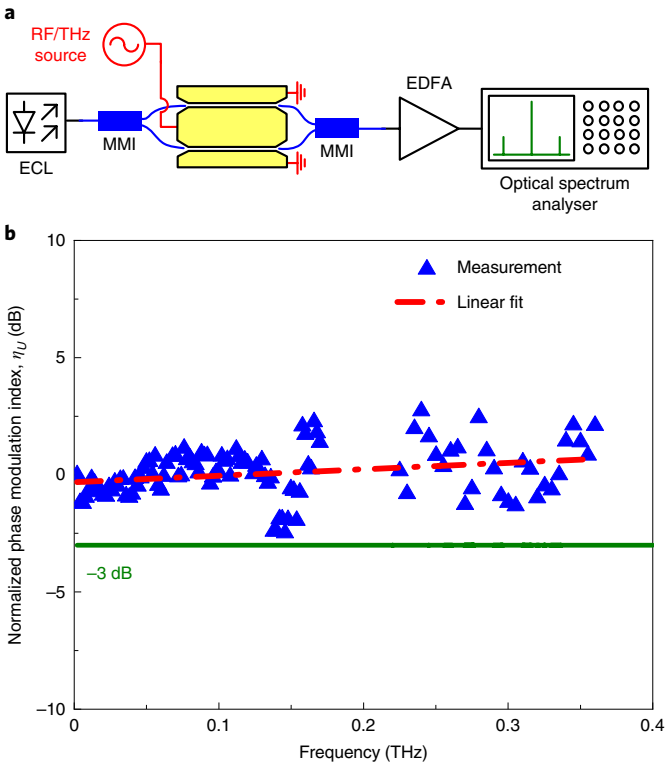

Fig. 2 | Bandwidth measurement of POH modulator. a, Experimental set-up for measuring the frequency-dependent phase modulation index η of the POH MZM. The c.w. light from an ECL is coupled to the modulator, which is driven by a RF/THz signal. The resulting optical spectrum is recorded by an optical spectrum analyser and the phase modulation index is extracted from the power ratio of the modulation sidebands and the c.w. carrier. **b**, Frequency dependence of the normalized modulation index η_U according to equation (1). The POH MZM features an ultra-broad frequency response up to at least 0.36 THz and shows no indication of a bandwidth limitation. The gap between 0.17 THz and 0.22 THz is due to the lack of a signal source in this frequency range.

For the THz wireless transmission experiments, we use a second-generation device with slightly longer phase shifter sections (20 µm instead of 15 µm) featuring a slot width of 75 nm and the same EO material (SEO100) as the cladding. For this device, we measured an EO figure-of-merit (FoM) of $n_{EO}^3 r_{33} = 315$ pm V^{-1}, leading to an estimated EO coefficient of $r_{33} = 64$ pm V^{-1}. Note that there is vast room to further improve the EO FoM and to hence reduce the drive voltage requirement by using more efficient EO materials. As an example, EO FoM values of $n_{EO}^3 r_{33} = 1,990$ pm V^{-1} (calculated for $n_{EO} = 1.83$ and $r_{33} = 325$ pm V^{-1}) have been previously demonstrated in POH devices[37], and even higher values of $n_{EO}^3 r_{33} = 2,300$ pm V^{-1} ($r_{33} = 390$ pm V^{-1} for $n_{EO} = 1.81$) have recently been achieved in silicon–organic hybrid modulators[38]. Moreover, the plasmonic losses of the modulator can be greatly reduced by, for example, using silver for the plasmonic slot waveguide. Together with the highly efficient EO polymers, this may lead to more than a 25-fold improvement in the π–voltage-loss product of the POH MZM (see Supplementary Sections V and VI for more details).

Figure 3a shows photographs of the experimental set-ups used for the transmission experiment. The THz Tx comprises a high-speed UTC photodiode with a horn antenna to generate the THz signal as well as a plano-convex polytetrafluoroethylene (PTFE) lens that collimates the THz beam. After travelling over a free-space distance of ~16 m, the THz signal is coupled to the POH MZM (not shown) through a second lens, a horn antenna and a two-stage THz amplifier. A more detailed description of the THz components and a technical sketch of the experimental set-up are provided in Supplementary Sections II and III, respectively. In the transmission experiment, a quadrature phase-shift keying (QPSK) data stream at a symbol rate of 15 GBd is encoded on an optical carrier at $f_0 = 193.3$ THz and superimposed with a c.w. LO tone at $f_{Tx,LO}$. Photomixing in the UTC photodiode is used to transfer the optical data stream to a THz carrier frequency of $f_{Tx,THz} = |f_0 - f_{Tx,LO}| = 0.2885$ THz. Figure 3b shows the optical spectrum at the input of the UTC photodiode, marked as position 'A' in Fig. 1b. At the THz Rx, the received signal is boosted by two cascaded THz amplifiers to drive the POH MZM via a GSG probe connected through a hollow-core waveguide. The amplifiers are based on millimetre-wave monolithic integrated circuits (MMIC) and provide a total gain of ~40 dB for frequencies between 0.270 THz and 0.310 THz (see Supplementary Section II for details). The POH MZM is biased at its quadrature (3 dB) point and hence imposes an intensity modulation on the c.w. carrier at $f_{Rx,LO} = 194.574$ THz obtained from another ECL. The optical data signal is amplified by EDFAs and sent through an optical filter, which suppresses the carrier at $f_{Rx,LO}$ along with the upper modulation sideband. The corresponding spectrum taken after the optical filter, that is, at position 'B' in Fig. 1c, is displayed in Fig. 3c. The optical QPSK signal is detected and evaluated using an optical modulation analyser with a built-in optical LO for coherent intradyne reception. Note that intensity-modulating a THz QPSK signal onto an optical carrier and selective filtering of one of the sidebands generates an optical QPSK signal even though the THz Rx contains only a simple MZM. Note also that, due to the limited tuning range of the optical filter, we chose to isolate the lower sideband of our optical signal rather than the upper one, as sketched in Fig. 1c.

The QPSK data signal is analysed offline using standard DSP techniques, and the bit error ratio (BER) is extracted. Figure 3d shows the BER as a function of the QPSK symbol rate, where the filled red triangles indicate the measured BER and the filled blue circles correspond to the BER estimated from the signal-to-noise (SNR) power ratio of the T/O converted signal. This estimate becomes unreliable for BER < 10^{-5} which are represented by blue open circles (see Supplementary Section IV for more details). Up to 18 GBd (line rate 36 Gbit s^{-1}), the BER stays below the 7% hard-decision forward error correction (FEC) limit[39], while we have to resort to a 20% soft-decision FEC for higher symbol rates. For higher symbol rates, the BER agrees well with estimations from the SNR, and is mainly limited by the amplified spontaneous emission (ASE) noise of the first EDFA after the POH MZM (EDFA 1 in Supplementary Fig. 7b). For smaller symbol rates, however, the measured BER differs greatly from the SNR-based (unreliable) estimations due to phase noise of the LO laser in the coherent optical receiver and due to nonlinear distortions caused by the THz amplifiers (see Supplementary Section IV for a detailed analysis). Figure 3e shows the QPSK constellations for line rates of 20, 30, 40 and 50 Gbit s^{-1}, respectively.

In summary, we have demonstrated an optical–wireless–optical link with purely optoelectronic frequency conversion both at the THz transmitter and the THz receiver. The link spans a distance of 16 m and is operated at a carrier frequency of 0.2885 THz. Key for this demonstration is a compact ultra-broadband POH modulator offering an ultra-high modulation bandwidth of more than 0.36 THz. With a 20% soft-decision FEC, we achieve a fibre-to-fibre line rate of 50 Gbit s^{-1}. In our current experiments, the transmission distance is limited to 16 m due to the width of our building. Further device improvements will allow to extend the scheme to transmission distances of 1 km or more, while still maintaining a reasonable loss margin (see Supplementary Section VI for details). These results demonstrate the prospects of POH modulators as powerful subsystems for THz receiver front-ends. Such devices lend themselves to co-integration with the full portfolio of silicon photonic

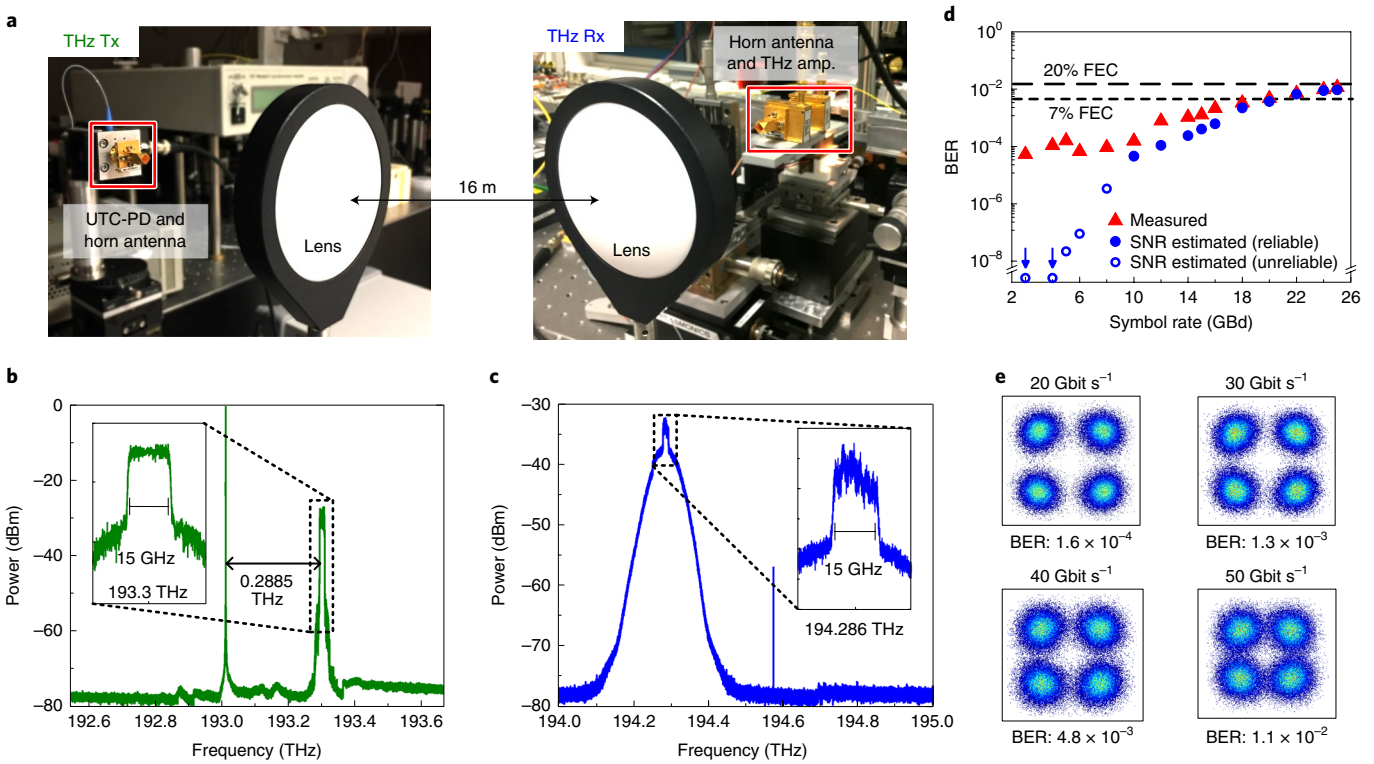

Fig. 3 | Demonstration of THz wireless data transmission using direct O/T and T/O conversion. a, Photograph of the THz transmitter (Tx) and receiver (Rx) set-up, separated by a distance of 16 m. The THz Tx comprises a high-speed UTC-PD, a horn antenna and a PTFE lens that collimates the THz beam. After travelling over a free-space distance of ~16 m, the signal is coupled to the POH MZM through a second lens, a horn antenna and a two-stage THz amplifier. A more detailed description and a technical sketch of the data transmission set-up are provided in Supplementary Section III and Supplementary Fig. 7. **b**, Optical spectrum measured at position 'A' of the THz Tx shown in Fig. 1b. The spectrum consists of a 15 GBd QPSK data signal (inset) at a carrier frequency of 193.3 THz and a c.w. tone, detuned from the carrier of the data signal by the targeted THz carrier frequency of 0.2885 THz. The THz signal is generated by photomixing in a UTC-PD. **c**, Filtered optical spectrum measured at position 'B' of the THz Rx (Fig. 1c). After modulating the THz signal onto the optical carrier, the upper sideband and the carrier are suppressed by an optical BPF such that only the lower sideband and the residual carrier are visible. The lower sideband contains a 15 GBd QPSK signal (inset) centred at 194.286 THz. **d**, BERs of QPSK signals at different symbol rates upon T/O conversion and coherent intradyne detection. Filled red triangles indicate measured BER obtained from 10^5 symbols of the received signal, whereas filled blue circles correspond to BER estimated from the SNR inthe signal bandwidth. For BER < 10^{-5} this estimate becomes increasingly unreliable—the associated BER values are indicated by blue open circles. The measured BER for higher symbol rates (>8 GBd) fit the estimations well. For lower symbol rates, the measured BER differs strongly from the (unreliable) estimations due to phase noise of the LO laser in the coherent optical receiver and due to nonlinear distortions caused by the THz amplifiers (see Supplementary Section IV for details). The BER stays below the 7% hard-decision FEC limit up to a symbol rate of 18 GBd. Higher symbol rates require 20% soft-decision FEC. **e**, Constellation diagrams of the received QPSK signal for data rates of 20, 30, 40 and 50 Gbit s^{-1}.

components that have emerged over recent years[30], possibly complemented by silicon-based nanoelectronic devices[31]. We believe that direct T/O conversion at the Rx can boost THz wireless links to data rates of hundreds of Gbit s^{-1}.

Online content

Any methods, additional references, Nature Research reporting summaries, source data, statements of code and data availability and associated accession codes are available at https://doi.org/10.1038/s41566-019-0475-6.

Received: 21 October 2018; Accepted: 22 May 2019;
Published online: 15 July 2019

References

1. Nagatsuma, T., Ducournau, G. & Renaud, C. C. Advances in terahertz communications accelerated by photonics. *Nat. Photon.* **10**, 371–379 (2016).
2. Kürner, T. & Priebe, S. Towards THz communications—status in research, standardization and regulation. *J. Infrared Millim. Terahertz Waves* **35**, 53–62 (2014).
3. Seeds, A. J., Shams, H., Fice, M. J. & Renaud, C. C. Terahertz photonics for wireless communications. *J. Lightwave Technol.* **33**, 579–587 (2015).
4. *Cisco Visual Networking Index: Forecast and Methodology, 2016–2021*, White Paper 22 (Cisco, 2017); http://www.cisco.com/c/en/us/solutions/collateral/service-provider/visual-networking-index-vni/complete-white-paper-c11-481360.pdf
5. Chow, C. W. et al. 100 GHz ultra-wideband (UWB) fiber-to-the-antenna (FTTA) system for in-building and in-home networks. *Opt. Express* **18**, 11–15 (2010).
6. Koenig, S. et al. Wireless sub-THz communication system with high data rate. *Nat. Photon.* **7**, 977–981 (2013).
7. Yu, X. et al. 160 Gbit/s photonics wireless transmission in the 300–500 GHz band. *APL Photon.* **1**, 081301 (2016).
8. Pang, X. et al. 260 Gbit/s photonic–wireless link in the THz band. In *Proceedings of 2016 IEEE Photonics Conference (IPC)* 9–10 (IEEE, 2016).
9. Beling, A. & Campbell, J. C. InP-based high-speed photodetectors. *J. Lightwave Technol.* **27**, 343–355 (2009).
10. Kanno, A. et al. Coherent terahertz wireless signal transmission using advanced optical fiber communication technology. *J. Infrared Millim. Terahertz Waves* **36**, 180–197 (2015).
11. Nagatsuma, T. et al. Terahertz wireless communications based on photonics technologies. *Opt. Express* **21**, 23736 (2013).
12. Wang, C. et al. 0.34-THz wireless link based on high-order area network applications. *IEEE Trans. Terahertz Sci. Technol.* **4**, 75–85 (2014).

13. Crowe, T. W. GaAs Schottky barrier mixer diodes for the frequency range 1–10 THz. *Int. J. Infrared Millim. Waves* **10**, 765–777 (1989).
14. Harter, T. et al. 110-m THz wireless transmission at 100 Gbit/s using a Kramers–Kronig Schottky barrier diode receiver. In *Proceedings of 44th European Conference on Optical Communication (ECOC'18)* Th3F.7 (postdeadline paper) (IEEE, 2018).
15. Ummethala, S. et al. Terahertz-to-optical conversion using a plasmonic modulator. In *Proceedings of Conference on Lasers and Electro-Optics* STu3D.4 (Optical Society of America, 2018).
16. Ummethala, S. et al. Wireless transmission at 0.3 THz using direct THz-to-optical conversion at the receiver. In *Proceedings of 44th European Conference on Optical Communication (ECOC'18)* We4H.3 (Optical Society of America, 2018).
17. Melikyan, A. et al. High-speed plasmonic phase modulators. *Nat. Photon.* **8**, 229–233 (2014).
18. Haffner, C. et al. All-plasmonic Mach–Zehnder modulator enabling optical high-speed communication at the microscale. *Nat. Photon.* **9**, 525–528 (2015).
19. Salamin, Y. et al. Direct conversion of free space millimeter waves to optical domain by plasmonic modulator antenna. *Nano Lett.* **15**, 8342–8346 (2015).
20. Melikyan, A. et al. Plasmonic–organic hybrid (POH) modulators for OOK and BPSK signaling at 40 Gbit/s. *Opt. Express* **23**, 9938–9946 (2015).
21. Ayata, M. et al. High-speed plasmonic modulator in a single metal layer. *Science* **358**, 630–632 (2017).
22. Haffner, C. et al. Low-loss plasmon-assisted electro-optic modulator. *Nature* **556**, 483–486 (2018).
23. Hoessbacher, C. et al. Plasmonic modulator with >170 GHz bandwidth demonstrated at 100 GBd NRZ. *Opt. Express* **25**, 1762–1768 (2017).
24. Macario, J. et al. Full spectrum millimeter-wave modulation. *Opt. Express* **20**, 810–815 (2012).
25. Wang, C. et al. Integrated lithium niobate electro-optic modulators operating at CMOS-compatible voltages. *Nature* **562**, 101–106 (2018).
26. Andrew, J. M. et al. Thin film lithium niobate electro-optic modulator with terahertz operating bandwidth. *Opt. Express* **26**, 14810–14816 (2018).
27. Veronis, G. & Fan, S. Modes of subwavelength plasmonic slot waveguides. *J. Lightwave Technol.* **25**, 2511–2521 (2007).
28. Veronis, G. & Fan, S. Guided subwavelength plasmonic mode supported by a slot in a thin metal film. *Opt. Lett.* **30**, 3359–3361 (2005).
29. Pile, D. F. P., Gramotnev, D. K., Oulton, R. F. & Zhang, X. On long-range plasmonic modes in metallic gaps. *Opt. Express* **15**, 13669 (2007).
30. Urbas, A. M. et al. Roadmap on silicon photonics. *J. Opt.* **18**, 073003 (2016).
31. Atabaki, A. H. et al. Integrating photonics with silicon nanoelectronics for the next generation of systems on a chip. *Nature* **556**, 349–354 (2018).
32. Pile, D. F. P. & Gramotnev, D. K. Adiabatic and nonadiabatic nanofocusing of plasmons by tapered gap plasmon waveguides. *Appl. Phys. Lett.* **89**, 041111 (2006).
33. Enami, Y., Luo, J. & Jen, A. K. Y. Short hybrid polymer/sol-gel silica waveguide switches with high in-device electro-optic coefficient based on photostable chromophore. *AIP Adv.* **1**, 042137 (2011).
34. Koos, C. et al. Silicon–organic hybrid (SOH) and plasmonic–organic hybrid (POH) integration. *J. Lightwave Technol.* **34**, 256–268 (2016).
35. Shi, Y., Yan, L. & Willner, A. E. High-speed electrooptic modulator characterization using optical spectrum analysis. *J. Lightwave Technol.* **21**, 2358–2367 (2003).
36. Naik, G. V., Shalaev, V. M. & Boltasseva, A. Alternative plasmonic materials: beyond gold and silver. *Adv. Mater.* **25**, 3264–3294 (2013).
37. Haffner, C. et al. Harnessing nonlinearities near material absorption resonances for reducing losses in plasmonic modulators. *Opt. Mater. Express* **7**, 2168–2181 (2017).
38. Kieninger, C. et al. Ultra-high electro-optic activity demonstrated in a silicon–organic hybrid (SOH) modulator. *Optica* **5**, 739–748 (2018).
39. Chang, F., Onohara, K. & Mizuochi, T. Forward error correction for 100 G transport networks. *IEEE Commun. Mag.* **48**, 48–55 (2010).

Acknowledgements

This work was supported by the European Research Council (ERC Consolidator Grant 'TeraSHAPE', no. 773248), the DFG project PACE (no. 403188360) within the Priority Programme 'Electronic–Photonic Integrated Systems for Ultrafast Signal Processing' (SPP 2111), the BMBF project SPIDER (no. 01DR18014A), the Alfried Krupp von Bohlen und Halbach Foundation, the Helmholtz International Research School of Teratronics (HIRST) and the Karlsruhe Nano Micro Facility (KNMF). We also thank J. Luo and A.K.-Y. Jen from Soluxra for providing the organic EO material.

Author contributions

S.U., T.H., W.F. and C.K. developed the concept and designed the experiment. S.U. and Z.L. designed the modulators and fabricated them with support from K.K., S.M., S.K.G., A.B. and L.H. S.U. and J.S. characterized the devices. S.U. and T.H. performed the transmission experiments and analysed the data together with J.K. and P.M.-P. Y.K. developed the poling procedure for the POH modulators and formulated the organic EO material. A.T. and M.W. developed and provided the THz MMIC amplifiers. The work was supervised jointly by T.Z., S.R., W.F. and C.K. S.U., W.F. and C.K. wrote the paper. All authors revised the paper.

Competing interests

The authors declare no competing interests.

Additional information

Supplementary information is available for this paper at https://doi.org/10.1038/s41566-019-0475-6.

Reprints and permissions information is available at www.nature.com/reprints.

Correspondence and requests for materials should be addressed to S.U. or C.K.

Publisher's note: Springer Nature remains neutral with regard to jurisdictional claims in published maps and institutional affiliations.

Methods

Fabrication and characterization of plasmonic–organic hybrid modulators. The POH modulators used in our experiments are fabricated on standard silicon-on-insulator substrates, featuring a 220-nm-thick silicon (Si) device layer and a 2-μm-thick buried oxide (SiO_2) layer. The structures are defined by high-resolution electron-beam lithography. A partial Si dry etch step and a subsequent full etch of the Si layer are used to form the grating couplers and the 500-nm-wide Si nanowire waveguides. The metallic slots of the plasmonic MZM are fabricated via a lift-off process in which a 150-nm-thick gold layer is thermally evaporated on a sacrificial layer of poly-methyl methacrylate (PMMA). The metallic slots in the two arms of the MZM are designed to be identical, each featuring a width of $w = 75$ nm (Fig. 1e). At the plasmonic section of the MZM, the Si nanowire waveguide (blue, Fig. 1e) ends with a tapered tip angle of 12° (inset, Fig. 1e). These tapers enable efficient conversion between the photonic mode in the silicon waveguide and the SPP in the metallic slot, with typical conversion losses of only 0.7 dB per transition[17]. The silicon waveguides in the two arms of the MZM have a geometrical length difference of 80 μm to enable adjustment of the MZM operating point by tuning the wavelength. The EO cladding consists of commercially available material SEO100, for which an EO coefficient of $r_{33} = 160\,\mathrm{pm\,V^{-1}}$ has been demonstrated in a thin-film experiment[33]. The EO material is spin-coated onto the plasmonic MZM and a static electric field is applied across the floating ground electrodes at an elevated temperature to align the randomly oriented dipoles of the EO material[34]. Subsequent cooling preserves the dipole orientation even after removal of the poling field. For a plasmonic slot waveguide length of $L = 20$ μm, we measured an insertion loss of 16 dB. The in-device EO FoM and the EO coefficient are estimated to be $n_{EO}^3 r_{33} = 315\ \mathrm{pm\ V^{-1}}$ and $r_{33} = 64\,\mathrm{pm\,V^{-1}}$, respectively, by assuming[33] $n_{EO} = 1.7$. These values are obtained from the measured $U_\pi L$-product of 240 V μm of the push–pull-operated MZM using the relation $U_\pi L = w\lambda_c / (2 n_{EO}^3 r_{33} \Gamma_{slot})$ (equation (7) in ref. [34]). In this equation, $\lambda_c = 1.55$ μm is the operating wavelength and U_π is the measured peak-to-peak modulation voltage that is needed to drive the MZM from constructive to destructive interference at low frequencies. The calculated field interaction factor $\Gamma_{slot} = 0.77$ (equation (20) in ref. [34]) describes the interaction between the modulating RF field and the optical field. By measuring on-chip silicon nanowire waveguides of different lengths at an excitation wavelength of 1.55 μm, we estimate an insertion loss of 6.5 dB per on-chip grating coupler and a propagation loss of 0.9 dB mm^{-1} for the silicon waveguide sections.

Bandwidth measurement. The frequency response of the plasmonic modulator is measured by applying a small sinusoidal voltage with variable frequency in the range $2\ \mathrm{GHz} \le f_m \le 0.36$ THz. The open-circuit transmission line electrodes of the POH MZM feature a total length of ~150 μm (see Supplementary Section I for details). For evaluation of the data, we use a global normalization technique that allows us to infer the overall shape of the frequency response despite strong variations in the electrical drive power for various frequency bands. The modulation signal is coupled to the POH MZM by GSG probes, which have a wave impedance of $Z = 50\,\Omega$. The open-circuit peak voltage U_e at the terminals of the POH MZM is estimated from the electric drive power P_e, which is available at the input of the GSG probe and is measured by replacing the probes by a power meter (see Supplementary Section I for details). To determine the phase modulation index η, we use a high-resolution optical spectrum analyser (APEX AP2050) to determine the power of the carrier f_c and of the two first-order intensity modulation sidebands at $f_c \pm f_m$. For larger drive amplitudes, a multitude of modulation sidebands would become visible at frequencies $f_c \pm k f_m$ ($k = 1, 2, 3, \ldots$). Assuming equal phase modulation indices η in both arms, the optical power at each frequency is given by[35] $P_o(f_c + k f_m) = P_i J_k^2(\eta)(1 + (-1)^k \cos\Delta\phi)$, where P_i is the power of the light entering the modulator, $J_k(\eta)$ is the kth-order Bessel function of the first kind, and $\Delta\phi$ is the phase difference between the two interferometer arms of the MZM that determines the operating point. The sideband-to-carrier power ratio of the first-order sidebands at $f_c \pm f_m$ and the spectral line at f_c is hence given by $R_{1,0} = P_o(f_c \pm f_m)/P_o(f_c) = \alpha J_1^2(\eta)/J_0^2(\eta)$ where $\alpha = (1 - \cos(\Delta\phi))/(1 + \cos(\Delta\phi))$. For small amplitudes of the modulating signal ($\eta \ll 1$), the Bessel functions can be approximated by $J_0(\eta) = 1$ and $J_1(\eta) = \eta/2$, which leads to $R_{1,0} \approx \alpha\eta^2/4$ (Supplementary Section I). To cover the frequency range of interest, we employ various sources: for $2\ \mathrm{GHz} \le f_m \le 64$ GHz, an Anritsu 37397C vector network analyser (VNA) is used, and a Keysight VNA (PNA-X, N5247) with different frequency extension modules (OML N5262-60003 and V06VNA2-T/R-A) acts as the RF source in the frequency ranges $70\ \mathrm{GHz} \le f_m \le 0.11$ THz and $0.11\ \mathrm{THz} \le f_m \le 0.17$ THz, respectively. The frequency range $0.22\ \mathrm{THz} \le f_m \le 0.36$ THz is covered by an electrical signal that is generated by photomixing of two detuned c.w. laser tones in a UTC photodiode. In the range $0.17\ \mathrm{THz} < f_m < 0.22$ THz, no source was available in our laboratory. To eliminate the impact of the frequency-dependent drive signal power, the modulation sidebands are measured together with the available electrical power P_e in front of the GSG probes, using a step size of 2 GHz for frequencies up to 0.17 THz and 5 GHz for frequencies from 0.22 THz to 0.36 THz. A dedicated calibration procedure is used to ensure global comparability of the modulation indices measured in the various frequency bands (equation (1); see Supplementary Section I for details). For frequencies up to 65 GHz, we use an Anritsu ML2438A power meter, whereas the power at higher frequencies is measured by a waveguide-coupled calorimeter (VDI Erickson PM4).

Data availability

The data that support the plots within this Letter and other findings of this study are available from the corresponding author(s) upon reasonable request.